



## Article

# Investigation of TiO<sub>2</sub> Deposit on SiO<sub>2</sub> Films: Synthesis, Characterization, and Efficiency for the Photocatalytic Discoloration of Methylene Blue in Aqueous Solution

Yuliana de Jesús Acosta-Silva <sup>1,\*</sup> , Manuel Toledano-Ayala <sup>1</sup>, Salvador Gallardo-Hernández <sup>2</sup>, Luis A. Godínez <sup>3</sup> and Arturo Méndez-López <sup>1,\*</sup>

<sup>1</sup> Research and Postgraduate Division, Faculty of Engineering, Autonomous University of Queretaro (UAQ), University Center, Querétaro 76010, Mexico

<sup>2</sup> Department of Physics, Center for Research and Advanced Studies of the National Polytechnic Institute, México City 07360, Mexico

<sup>3</sup> Centro de Investigación en Química para la Economía Circular, CIQEC, Faculty of Chemistry, Autonomous University of Queretaro, University Center, Querétaro 76010, Mexico

\* Correspondence: yuliana.dejesus.acosta@uaq.mx (Y.d.J.A.-S.); arturo.mendez@uaq.mx (A.M.-L.)

**Abstract:** TiO<sub>2</sub>-SiO<sub>2</sub> thin films were created on Corning glass substrates using a simple method. Nine layers of SiO<sub>2</sub> were deposited; later, several layers of TiO<sub>2</sub> were deposited, and their influence was studied. Raman spectroscopy, high resolution transmission electron spectroscopy (HRTEM), an X-ray diffractometer (XRD), ultraviolet-visible spectroscopy (UV-Vis), a scanning electron microscope (SEM), and atomic force microscopy (AFM) were used to describe the sample's shape, size, composition, and optical characteristics. Photocatalysis was realized through an experiment involving the deterioration of methylene blue (MB) solution exposed to UV-Vis radiation. With the increase of TiO<sub>2</sub> layers, the photocatalytic activity (PA) of the thin films showed an increasing trend, and the maximum degradation efficiency of MB by TiO<sub>2</sub>-SiO<sub>2</sub> was 98%, which was significantly higher than that obtained by SiO<sub>2</sub> thin films. It was found that an anatase structure was formed at a calcination temperature of 550 °C; phases of brookite or rutile were not observed. Each nanoparticle's size was 13–18 nm. Due to photo-excitation occurring in both the SiO<sub>2</sub> and the TiO<sub>2</sub>, deep UV light ( $\lambda = 232$  nm) had to be used as a light source to increase photocatalytic activity.

**Keywords:** dip-coating; TiO<sub>2</sub>-SiO<sub>2</sub> thin films; photocatalytic processes; methylene blue; sol-gel; UV-visible light



**Citation:** Acosta-Silva, Y.d.J.; Toledano-Ayala, M.; Gallardo-Hernández, S.; Godínez, L.A.; Méndez-López, A. Investigation of TiO<sub>2</sub> Deposit on SiO<sub>2</sub> Films: Synthesis, Characterization, and Efficiency for the Photocatalytic Discoloration of Methylene Blue in Aqueous Solution. *Nanomaterials* **2023**, *13*, 1403. <https://doi.org/10.3390/nano13081403>

Academic Editors: Ricardo Lopez Anton, Jose Maria De Teresa and Sion Federico Olive Méndez

Received: 13 March 2023  
Revised: 5 April 2023  
Accepted: 11 April 2023  
Published: 19 April 2023



**Copyright:** © 2023 by the authors. Licensee MDPI, Basel, Switzerland. This article is an open access article distributed under the terms and conditions of the Creative Commons Attribution (CC BY) license (<https://creativecommons.org/licenses/by/4.0/>).

## 1. Introduction

Diverse colors and other organic and inorganic contaminants are found in textile industry wastewater. Twelve percent of synthetic textile dyes, including eriochrome black-T (EBT), methyl orange (MO), rhodamine B, and methylene blue (MB), are thought to be lost during the dyeing process, and approximately 20% of these dyes are carried as waste to industrial wastewater treatment facilities [1]. Among these chemicals, MB is one of the most popular, as it is used not only as a dye for wool, hair coloring compounds, paper prints, and cotton, but also as an antiseptic, among other health-related purposes [2]. MB, on the other hand, is regarded as biologically dangerous, because it is a powerful carcinogen for marine animals, and in humans severely irritates the eyes, causes convulsions, irritates sensitive skin, and induces tachycardia [3]. MB also reacts with various substances, which makes the treatment of aqueous effluents containing MB a difficult task [4]. On the other hand, advanced oxidation processes (AOPs) are regarded as efficient approaches for the elimination of organic contaminants from aqueous solutions, such as MB. These procedures are based on the fact that hydroxyl radicals (HO●), which have a particularly high oxidation potential, rapidly oxidize the majority of organic contaminants

with great efficiency (generally in the range  $108\text{--}1011\text{ M}^{-1}\text{ s}^{-1}$ ) [5–7]. One way to produce OH radicals is by the oxidation of surface adsorbed  $\text{H}_2\text{O}$  molecules, using photo-excited semiconductor materials [8]. Titanium dioxide ( $\text{TiO}_2$ ) is an excellent photocatalyst, due to its low cost, nontoxicity, and good chemical and mechanical stability [9,10]. Therefore,  $\text{TiO}_2$  is used in solar cells [11], self-cleaning glasses [12], antifogging windows [13], and as a photocatalytic material for the degradation of contaminants in wastewater [14]. The ability of illuminated  $\text{TiO}_2$  to produce OH radicals depends on specific features of  $\text{TiO}_2$ , such as the size of the semiconductor crystallites and their surface area [15]. The photo-physical and chemical properties of the  $\text{TiO}_2$  material allows for coupling to other semiconductors; in this regard,  $\text{SiO}_2$  is a practical option because of its great mechanical strength and good thermal stability [16]. Amorphous  $\text{SiO}_2$  has also been demonstrated to have a high surface area and outstanding adsorption capacity, making it an effective substrate for semiconductor films [17]. Zhou et al., for example, demonstrated that mixed metal oxides ( $\text{TiO}_2\text{-SiO}_2$ ) improve the photocatalytic efficiency of the individual materials, because it enhances the materials' adsorption properties and increases their concentration of surface hydroxyl groups in the thin film. In addition,  $\text{SiO}_2$  was shown to promote a large surface area and an appropriately porous structure [15]. There are abundant reports in the literature focusing on the synthesis and characterization of  $\text{TiO}_2$ -based photocatalysts; in this context, we believe that in addition to phase structure, doping, and composite design and synthesis, the study of  $\text{TiO}_2$  layers grown by the sol-gel dip-coating method on top of the  $\text{SiO}_2$  semiconductor material films could be useful for the development of novel and efficient photocatalytic surfaces. This communication, therefore, presents the structural, morphological, and optical properties of the  $\text{SiO}_2/\text{TiO}_2$  composite films proposed, as well as an exploration of their photocatalytic performance.

## 2. Experimental Details

### 2.1. $\text{SiO}_2$ Thin Films

$\text{SiO}_2$  solutions were prepared by dissolving a certain amount of triblock copolymer (BASF, EO106-PO70-EO106, F127) in ethanol (J.T. Baker, Querétaro, Mexico), with constant stirring for 1 h at  $37\text{ }^\circ\text{C}$ . Then, 0.7 mL of HCl (J.T. Baker) were added by drops, and the solution was continuously stirred for 30 min. After adding 5.5 mL of TEOS to the mixture, it was agitated for 24 h at  $36\text{ }^\circ\text{C}$ . The resulting transparent and homogeneous phase was then employed to prepare thin films on glass substrates (Corning 2947, area  $2.5 \times 7.5\text{ cm}^2$ ) using the dip-coating technique. Figure 1a shows a scheme describing the dip-coating process employed in this work. The previously cleaned substrate is dipped into a solution of the precursors (the material to be deposited) and then withdrawn vertically at a controlled speed. For this purpose, the homemade system shown in Figure 1b (operating at a withdrawal rate of  $8\text{ cm/min}$ ) was utilized to obtain  $\text{SiO}_2$  thin films containing nine sequential coatings; each layer was prepared by drying the coating at  $250\text{ }^\circ\text{C}$  for 2 h in an open atmosphere. Subsequently, the temperature was increased to  $550\text{ }^\circ\text{C}$  (calcination temperature) over two hours at a rate of  $2\text{ }^\circ\text{C/min}$  ramp.

### 2.2. $\text{TiO}_2\text{-SiO}_2$ Thin Films

Thin films were prepared by immersion as reported in a previous section, in a solution containing titanium (IV) isopropoxide (Sigma-Aldrich Co., Querétaro, Mexico), 2-propanol (J.T. Baker), and hydrochloric acid (37% HCl). The  $\text{TiO}_2$  thin films were deposited using the  $2\text{ cm/min}$  removal rate for the dip coating process, and in this case, the films surveyed consisted of coatings of 5, 7, and 9 layers. As was indicated for the  $\text{SiO}_2$  films, each layer was dried at  $250\text{ }^\circ\text{C}$  for 3 min, and once each film was completed with the corresponding number of layers, the surface modified material was calcined at  $550\text{ }^\circ\text{C}$  for 1 h. In terms of the cross-sectional characterization of the composite films under study, we carried out thickness measurements using a KLA TENCO P-15 profilometer as described in the experimental section. In this way, while the thickness of the  $\text{SiO}_2$  films under study corresponded to

~250 nm, the thicknesses of the TiO<sub>2</sub> material films consisted of ~171, 219, and 262 nm, depending on the number of deposited TiO<sub>2</sub> layers (5, 7 and 9, respectively).

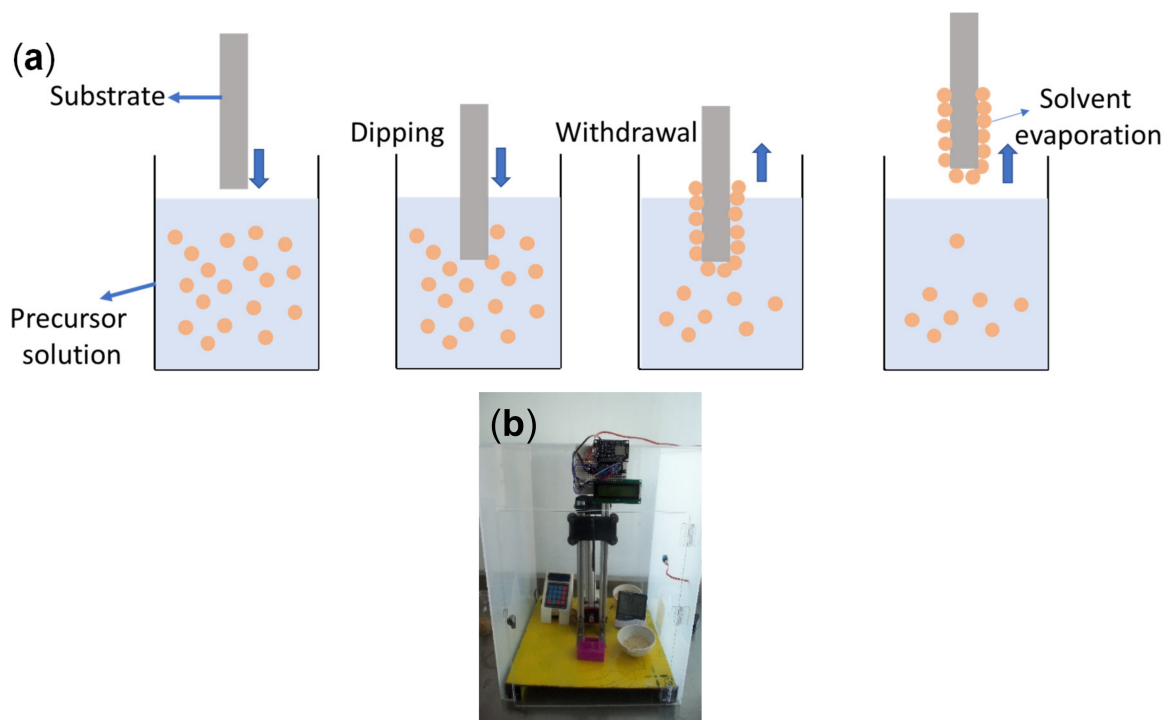


**Figure 1.** (a) Sequential steps of the sol-gel dip-coating method for thin film deposition. (b) Dip coating system assembled in the NanoBiotechnology and Photocatalysis Laboratory—UAQ. This system is used for the production of various thin films.

### 2.3. Structural, Optical, and Morphological Characterization of the Films

UV-Vis measurements were carried out using an Evolution 220 UV-Vis Spectrophotometer. X-ray diffraction experiments were carried out using a Philips X-ray diffractometer (PANalytical's X'pert PRO X-ray diffractometer, Malvern, UK) that employs a Cu-K $\alpha$  radiation with a  $\lambda$  of 0.15405 nm in the  $20 \leq 2\theta \leq 80^\circ$  range. The voltage and current settings were 30 kV and 40 mA, respectively. The samples were continuously scanned with a step size of  $0.02^\circ$  ( $2\theta$ ) and a count time of 1 s per step. Structural properties were also studied using Raman spectroscopy that collected data using a Labram-Dilor Raman spectrometer equipped with a He-Ne laser exciting source, operating between the wavelengths of 200 and 800 nm at ambient temperature (AT). The roughness and surface topography were examined by AFM (Park Scientific Inst. System, Suwon, South Korea). Using a scanning electron microscope (SEM, JEOL JSM-6300, Tokyo, Japan), surface pictures were acquired. Prior to the acquisition of images by high-resolution transmission electron microscopy, tiny bits of films were scraped. JEOL JEM 2010 microscope with an acceleration voltage of 200 kV was used for this objective. Typically, the magnification ranged from  $\times 400,000$  to  $\times 500,000$ . At the camera length  $L = 20$  cm, selected area electron diffraction (SAED) was carried out. Thickness measurements were made using a KLA TENCOR P-15 profilometer (Milpitas, CA, USA).

### 2.4. Photocatalytic Activity Evaluation

The PA of films was determined at AT by assessing the MB discoloration kinetics of aqueous solutions of 5.4 mg/L ( $1.88 \times 10^{-5}$  mol/L) under UV radiation. In this way, 3 mL of the aqueous MB solution were poured into a standard quartz cell, and later, a TiO<sub>2</sub>-SiO<sub>2</sub> coated substrate was placed vertically inside the cell (with a 2 cm<sup>2</sup> exposed area). Five quartz cells prepared in this way were used for each thin film under study. The 15 W

lamp used to produce the irradiation light had a 254 nm wavelength (G15T8 germicidal lamp as the exciting source). Five centimeters separated the quartz cells from the lamp. A Thermo Scientific™ Evolution 220 Spectrophotometer was used to measure the optical absorbance of the test solution every 60 min for the course of the 5 h of total irradiation. The absorbance peak reduction for MB was examined in the range of 400 to 800 nm. The residual methylene blue concentration was calculated using the absorbance data at 664 nm employing the Beer-Lambert's law.

### 3. Results and Discussion

#### 3.1. X-ray Diffraction

The XRD patterns of the thin films of TiO<sub>2</sub> deposited on mesoporous SiO<sub>2</sub> thin films are shown in Figure 2. The JCPDS-ICDD powder diffraction database was used to identify the crystal phases and matching miller indices. The JCPDF number for TiO<sub>2</sub> is 00-21-1272. The anatase phase of TiO<sub>2</sub> predominated in all the samples' patterns; no other phase was present. The samples diffraction peaks were seen at 2θ values of 25.3°, 37.8°, 38.6°, 48.1°, 53.9°, 55.1°, 62.7°, 68.9°, 70.4°, and 75.1° and could be perfectly correlated with the (101), (004), (112), (200), (105), (211), (204), (116), (220), and (215) crystal planes of anatase TiO<sub>2</sub>. All peaks were well indexed according to the standard patterns. The increase in the number of TiO<sub>2</sub> coatings resulted in thin films that exhibited higher intensities, indicating an increase in crystallinity owing to the higher presence of TiO<sub>2</sub> layers on top of SiO<sub>2</sub>. No phase transformation occurred for any of the samples. Moreover, all samples displayed a preferential orientation growth at (101) the plane (see Figure 2), which can be attributed to the plane's low surface energy value [18]. According to Zhang et al. [19], the phase transformation of TiO<sub>2</sub> only takes place at temperatures above 900 °C. An estimation of average crystallite size was calculated using the Scherrer equation; 5TiO<sub>2</sub>-9SiO<sub>2</sub>, 7TiO<sub>2</sub>-9SiO<sub>2</sub>, and 9TiO<sub>2</sub>-9SiO<sub>2</sub> samples correspond to 13, 14, and 18 nm, respectively. For these calculations, Equation (1) was used as follows [20]:

$$d = \frac{K\lambda}{\beta \cos \theta} \quad (1)$$

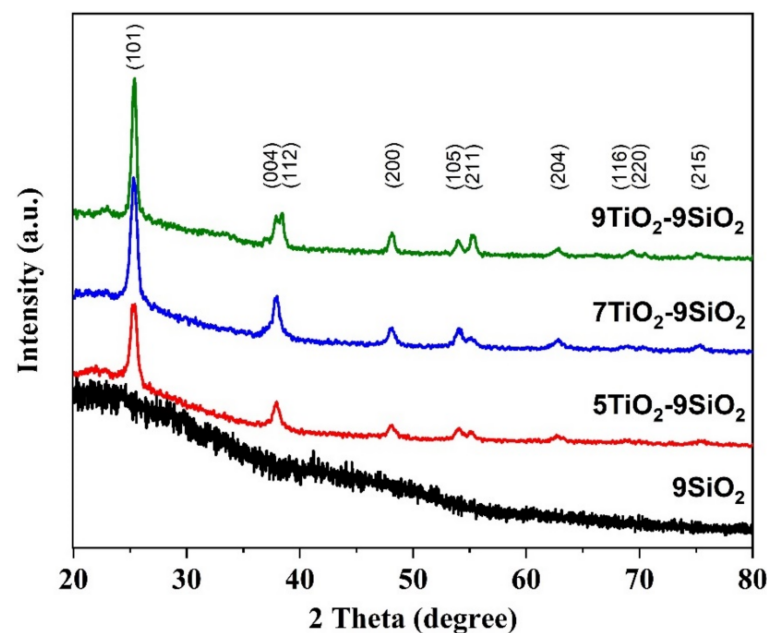


**Figure 2.** X-ray diffraction patterns for samples of TiO<sub>2</sub> over SiO<sub>2</sub> annealed. The tetragonal phase is linked to thin films of TiO<sub>2</sub> that correspond to the (hkl) indices.

$\lambda$  the wavelength of the radiation (1.54056 for CuK radiation),  $\theta$  is Bragg's angle,  $\beta$  the full width at half maximum (FWHM) intensity in radians,  $d$  the average thickness of the crystal in a direction normal to the diffracting plane (hkl), and  $K$  is Scherrer constant.

Equations (2) and (3), respectively, express two additional structural parameters known as the dislocation density ( $\delta$ ) and the microstrain ( $\epsilon$ ) [21]:

$$\delta = \frac{1}{d^2} \quad (2)$$

$$\epsilon = \frac{\beta}{4 \tan \theta} \quad (3)$$

Figure 3 illustrates how the number of layers of TiO<sub>2</sub> affected the variance in dislocation density, crystallite size, and strain in the thin films studied. The following values demonstrate that the strain decreases as the number of layers are enhanced and the crystallite size increases. The same trend of the crystallite size was also reported by Lin et al. [22] for ZnO films made with various thicknesses. The relationship between the two variables can be explained by the collective fusing of small crystallite particles into larger ones, which leads to decreased densities of nucleation centers and, in turn, internal strain [23,24].

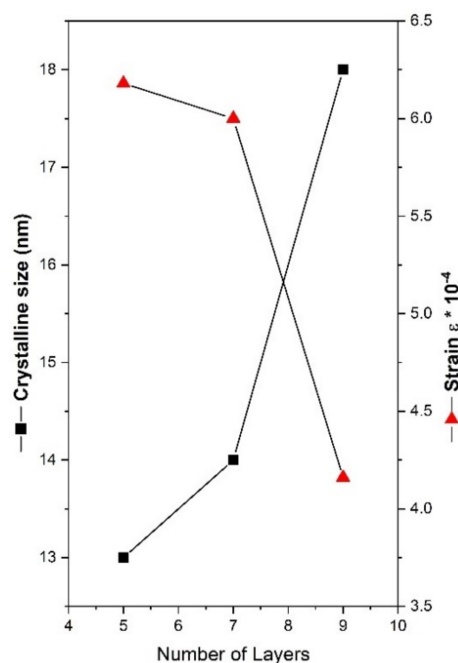


**Figure 3.** Crystallite size and strain of TiO<sub>2</sub>-SiO<sub>2</sub> thin films based on the quantity of dip-coating layers.

### 3.2. UV-Vis

Based on the UV-vis characterization experiments, transmittance (T), and reflectance (R) data on the TiO<sub>2</sub>-SiO<sub>2</sub> thin films were obtained in the 300–1100 nm wavelength window. Figure 4a–c shows that transmittance spectra are characterized by maxima and minima values of different orders. As the film thickness increases (to 5, 7, and 9 layers), the location of a particular transmittance extrema (maxima) shifts towards longer wavelengths. Similar results have been reported for five TiO<sub>2</sub> layers on SiO<sub>2</sub> [25]. Also, the thin films under investigation displayed a dramatic decline in transmittance in the ultraviolet spectrum. It was found that the absorption edge of the transmittance moves towards red in the ultraviolet region as the film thickness grows for TiO<sub>2</sub> thin films produced with the same withdrawal speed. Figure 4d shows the optical reflectance as a function of wavelength ( $\lambda$ ). When there is an increase in the number of layers, the reflectance rises, which is more significant within the visible region. The band gap between conduction (CB) and valence bands (VB), a crucial optical characteristic of thin films, is calculated using the well-known Tauc equation, as given in Equation (4) [26]:

$$\alpha h\nu = A(h\nu - E_g)^n \quad (4)$$

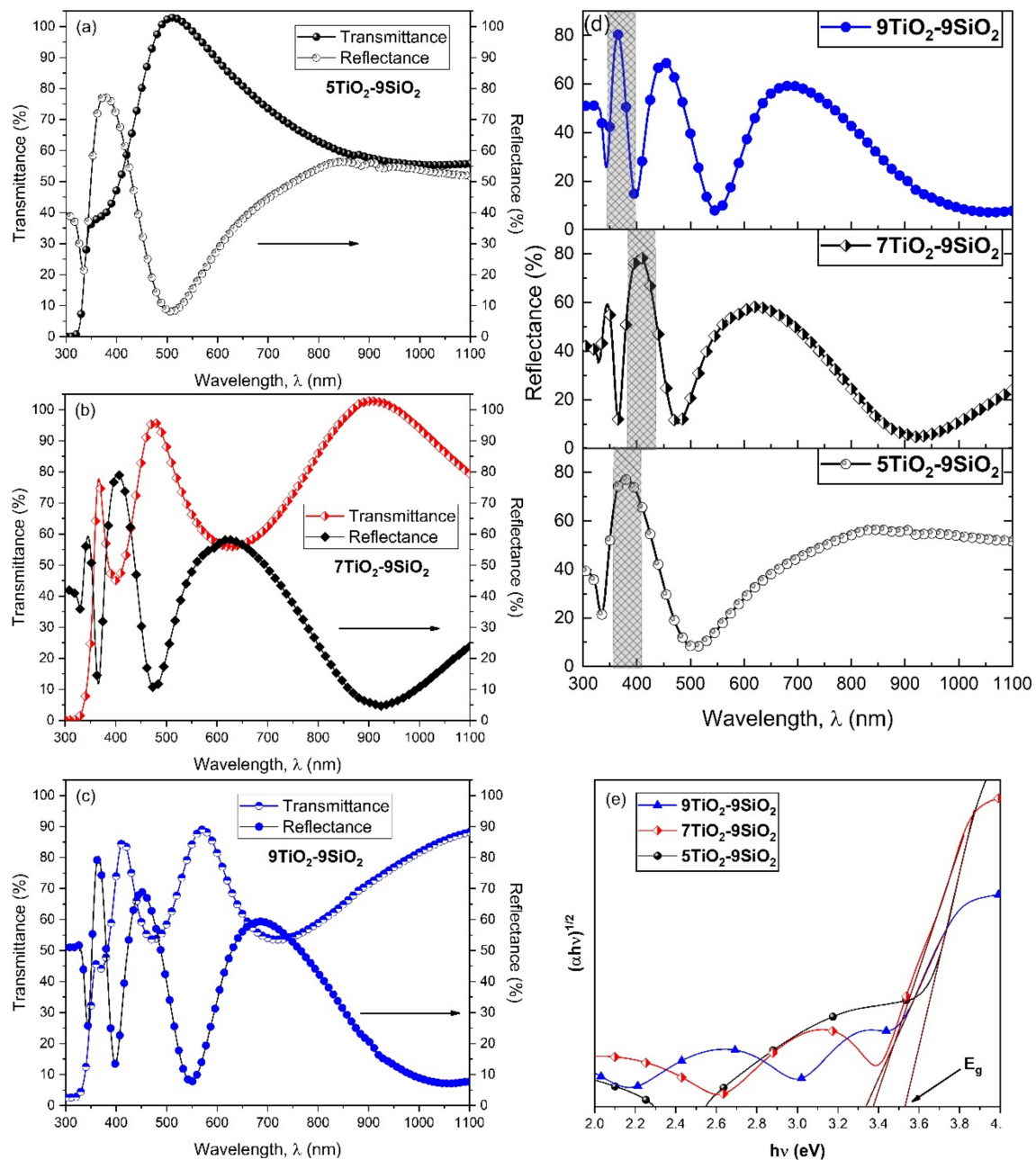


**Figure 4.** Determination of  $E_g$  energy for TiO<sub>2</sub>-SiO<sub>2</sub> thin films. (a–c) Spectral dependence of  $T(\lambda)$  and  $R(\lambda)$  coefficients, (d) UV-Visible reflectance spectra of TiO<sub>2</sub>-SiO<sub>2</sub> thin films, (e)  $E_g$  determined by optical method using  $(\alpha h\nu)^{1/2}$  vs.  $h\nu$  plots of thin films deposited with different numbers of TiO<sub>2</sub>-SiO<sub>2</sub> layers.

Here, the constant  $A$  is related to the effective masses (electrons and holes), the input photon energy is represented by  $h\nu$ , the optical bandgap is represented by  $E_g$ , and the exponent  $n$  is dependent on the kind of transition. When  $n = 2$  denotes permitted indirect transitions, 3 denotes forbidden indirect transitions, 1/2 denotes permissible direct transitions and 3/2 for forbidden direct transitions. When the line is intercepted at the energy axis ( $\alpha = 0$ ) yields the band gap (Figure 4e). Here, it can be shown that the  $E_g$  values decrease as the number of TiO<sub>2</sub> layers increases. The  $E_g$  value for 9TiO<sub>2</sub>-9SiO<sub>2</sub> was found to be 3.34 eV, as shown in Figure 4e, which is comparable to observations reported by other groups [27–29]. The bandgap energy in Figure 4e for 5TiO<sub>2</sub> is 3.53 eV, and in this regard, it has been reported that for powders light absorption (as well as the bandgap of TiO<sub>2</sub>), does

not change when several layers of TiO<sub>2</sub> are present. For interacting semiconductor layers, however, it is common to observe a decrease in the band gap due to an increase in the grain size of TiO<sub>2</sub> layers [30]. Also, some sub-bands form due to defect levels in the forbidden band of TiO<sub>2</sub>, thereby reducing the “band-gap energy” [31].

### 3.3. Raman Spectroscopy

Raman measurements of the layers of TiO<sub>2</sub> deposited on mesoporous SiO<sub>2</sub> were investigated as described in the experimental section. The resulting Raman data in the 190–800 cm<sup>-1</sup> range (Figure 5) show that the anatase titania vibrational modes E<sub>g</sub>, B<sub>1g</sub>, A<sub>1g</sub>+B<sub>1g</sub>, and E<sub>g</sub> have been assigned to peaks at 197, 394, 516, and 637 cm<sup>-1</sup> in all samples, respectively [32,33]. While the peaks located at 197 and 637 cm<sup>-1</sup> agree with the E<sub>g</sub> mode (attributed to the symmetric stretching vibration of O-Ti-O) and a B<sub>1g</sub> mode corresponds to the peak at 394 cm<sup>-1</sup> (which is due to the symmetric bending vibration of O-Ti-O), the A<sub>1g</sub> mode arises from the asymmetric bending vibration of this same bond. The latter mode also overlaps with the remaining B<sub>1g</sub> mode, producing the emission of a signal with a peak at 516 cm<sup>-1</sup>. This mode was extensively investigated by Otakar et al. [33]. The intensity of the peaks is normally affected by the number of layers [34]. The Raman spectra obtained indicate that the surface of the TiO<sub>2</sub> thin films is characterized by a pure anatase phase without the production of impurity phases, because there are no rutile (447 and 612 cm<sup>-1</sup>) [35] or brookite (246 and 449 cm<sup>-1</sup>) [36] phase peaks present. As was previously discussed, these results are consistent with XRD data.

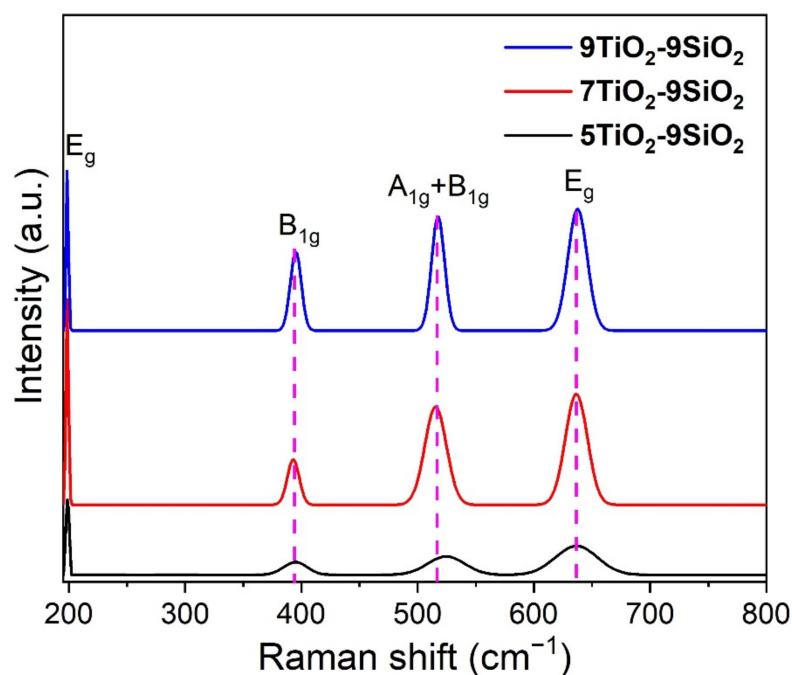


**Figure 5.** Raman spectrum of TiO<sub>2</sub>-SiO<sub>2</sub> thin films heated to 550 °C in air (anatase).

### 3.4. Atomic Force Microscopy (AFM)

The TiO<sub>2</sub>-SiO<sub>2</sub> thin films that were deposited on Corning glass are depicted in Figure 6 in both two- and three-dimensional AFM pictures. The surface morphologies of the films under study reveals porous structures that, interestingly, are characterized by different roughness. Figure 6a shows that 5TiO<sub>2</sub>-9SiO<sub>2</sub> films are composed by monodisperse spherical particles of a diameter 3.683 nm with a mesoporous structure [37,38]. The main benefit of the reverse micellar route by hydrolysis of titanium isopropoxide to produce TiO<sub>2</sub> nanoparticles is monodispersity [39]. In this way, the hydration of surfactant polar heads by water molecules is in competition with the hydrolysis process. Growth restrictions and homogeneous particle sizes are caused by the surfactant molecule restructuring that surround

the polar species produced during hydrolysis [37]. It is also observed from Figure 6b,c that the 7TiO<sub>2</sub>-9SiO<sub>2</sub> and 9TiO<sub>2</sub>-9SiO<sub>2</sub> thin films also have granular microstructures which are composed of ~4.53 nm and ~8.43 nm spheric crystals, respectively. AFM image analysis showed the values of surface roughness in addition to crystal diameter. The root mean square roughness values ( $R_{rms}$ ) of 5TiO<sub>2</sub>-9SiO<sub>2</sub>, 7TiO<sub>2</sub>-9SiO<sub>2</sub> and 9TiO<sub>2</sub>-9SiO<sub>2</sub> correspond to 0.508, 0.177 and 0.076 nm, respectively.

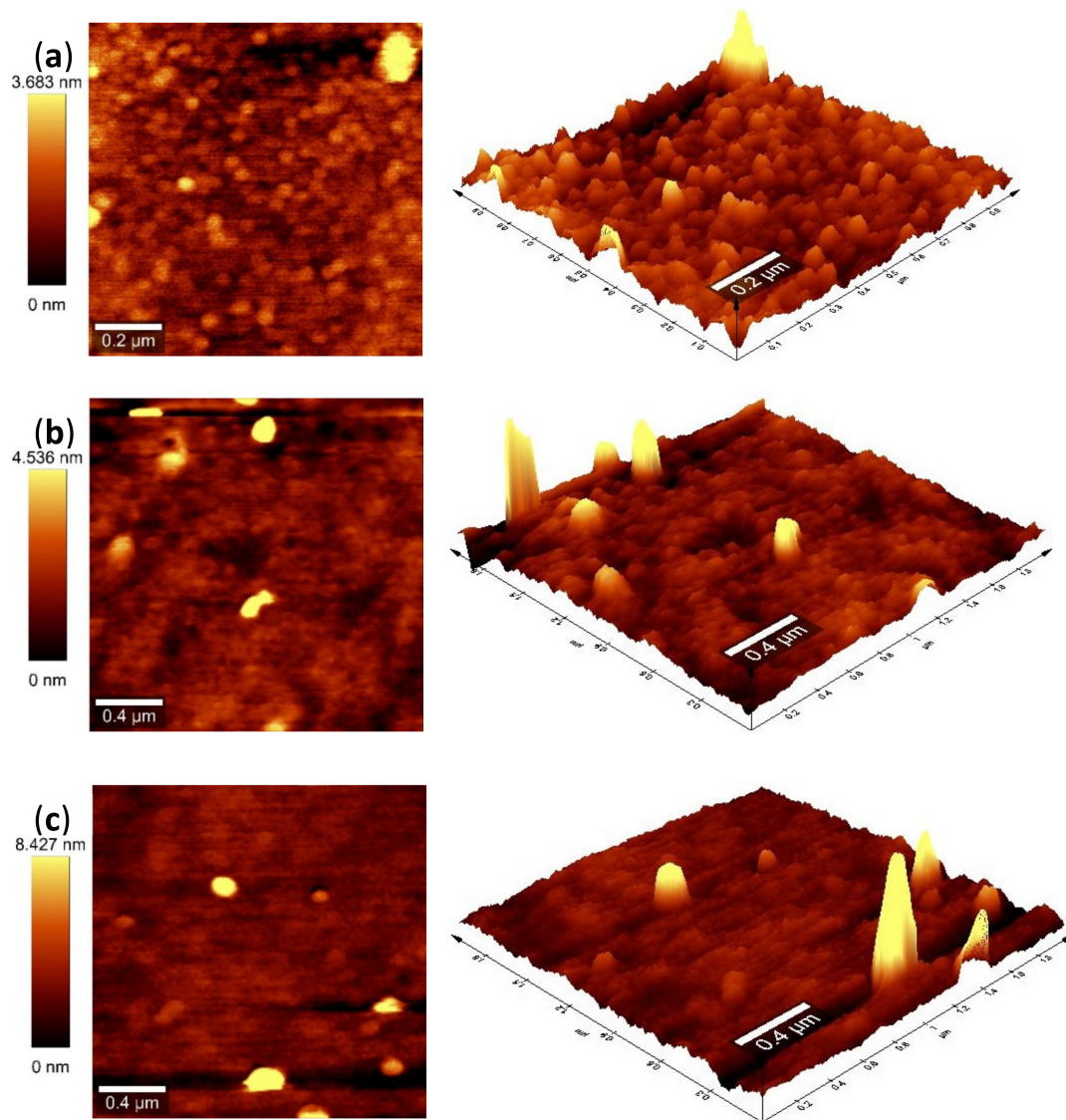


**Figure 6.** 2- and 3-dimensional images of TiO<sub>2</sub>-SiO<sub>2</sub> thin films with different numbers of layers. (a) 5TiO<sub>2</sub>-9SiO<sub>2</sub> (5 layers), (b) 7TiO<sub>2</sub>-9SiO<sub>2</sub> (7 layers), and (c) 9TiO<sub>2</sub>-9SiO<sub>2</sub> (9 layers).

### 3.5. Scanning Electron Microscope (SEM)

Figure 7 shows the micrographs of thin films. The films under study were annealed at 550 °C; it was observed that the shapes of the formed grains appear to vary according to the number of layers. The most significant differences between the three samples were observed for five layers of TiO<sub>2</sub> (Figure 7a), seven layers (Figure 7b), and nine layers (Figure 7c). We observed that by increasing the thickness of the TiO<sub>2</sub> films, crack formation did not take place, suggesting not only a relatively strong structure, but also that an increase in the film thickness did not lead to detachment of the deposited layers. For the 5TiO<sub>2</sub>-9SiO<sub>2</sub> thin film (Figure 7a), less closely packed TiO<sub>2</sub> particles were dispersed, and a sizable particle increase was observed. As the deposition of the layers in the 7TiO<sub>2</sub>-9SiO<sub>2</sub> sample

(Figure 7b) increased, densely packed and uniform nanoscale particles were observed; similar results have been reported in previous studies of  $\text{TiO}_2/\text{SiO}_2$  films [40]. The image of the  $9\text{TiO}_2\text{-}9\text{SiO}_2$  thin film (Figure 7c) shows an extremely smooth surface involving tiny and dense grains positioned on the surface of the film. These results are comparable to those mentioned by Binyu Yu et al. [41].

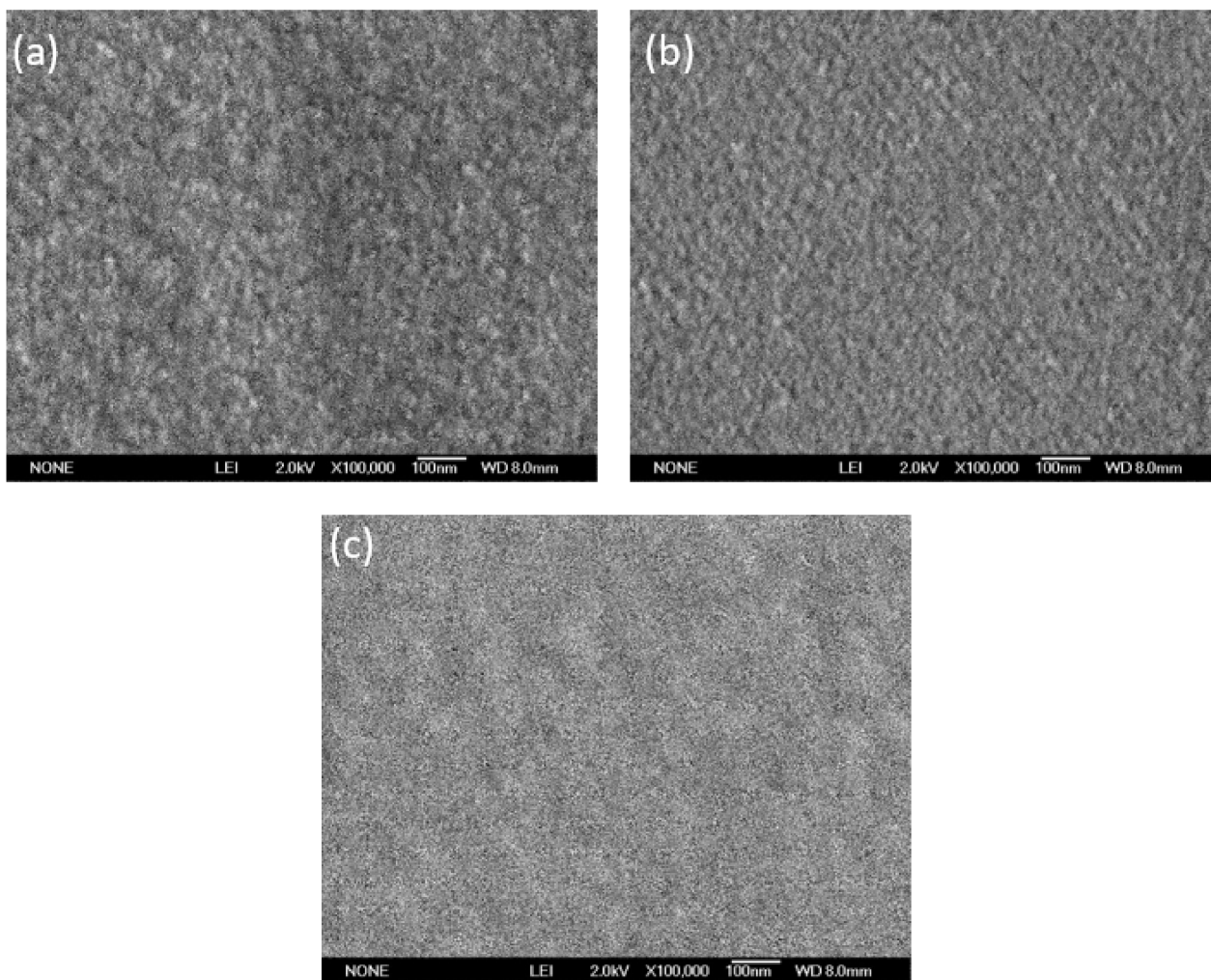


**Figure 7.** SEM pictures of: (a) sample  $5\text{TiO}_2\text{-}9\text{SiO}_2$ ; (b) sample  $7\text{TiO}_2\text{-}9\text{SiO}_2$ ; (c) sample  $9\text{TiO}_2\text{-}9\text{SiO}_2$ .

### 3.6. High Resolution Transmission Electron Spectroscopy (HRTEM)

$7\text{TiO}_2\text{-}9\text{SiO}_2$  thin films were examined using High-resolution TEM (HRTEM) to evaluate their crystalline or amorphous. Size distribution analysis shown in Figure 8a reveals that the average diameter and standard deviation of  $7\text{TiO}_2\text{-}9\text{SiO}_2$  nanoparticles on the surface of the film are about 3–5 nm—a value range that is not consistent with that calculated from XRD experiments. The Scherrer equation, however, is well known to produce a good approximation, and in this regard, the disordered wormhole-like pore structure of the dip-coating prepared sample was confirmed by TEM (see Figure 8b). This material is a good illustration of the type of molecular sieve in which the atomic organization is disordered similarly to amorphous or mesoporous silica, and the channel structure displays a disordered pattern of micropores with a high specific surface area. High-resolution TEM (HRTEM) images of  $7\text{TiO}_2\text{-}9\text{SiO}_2$  in Figure 8c–e revealed the crystalline nature of the nanostructures under study with lattice fringe spacing of 3.52 Å, 1.48 Å, and 1.66 Å, respectively. These can be indexed to (101), (204), and (211) planes of anatase  $\text{TiO}_2$ . Figure 8f, on the other hand, shows the transmission electron diffraction pattern of a  $7\text{TiO}_2\text{-}9\text{SiO}_2$  sample. From

electron diffraction measurements, the interplanar distances ( $d$ ) of  $7\text{TiO}_2\text{-9SiO}_2$  samples were determined to be 2.33 Å, 1.33 Å and 1.16 Å. This result corresponds to anatase phase of  $\text{TiO}_2$ . The interplanar distance and the diffraction planes were identified using the powder diffraction files (PDF) #00-021-1272.

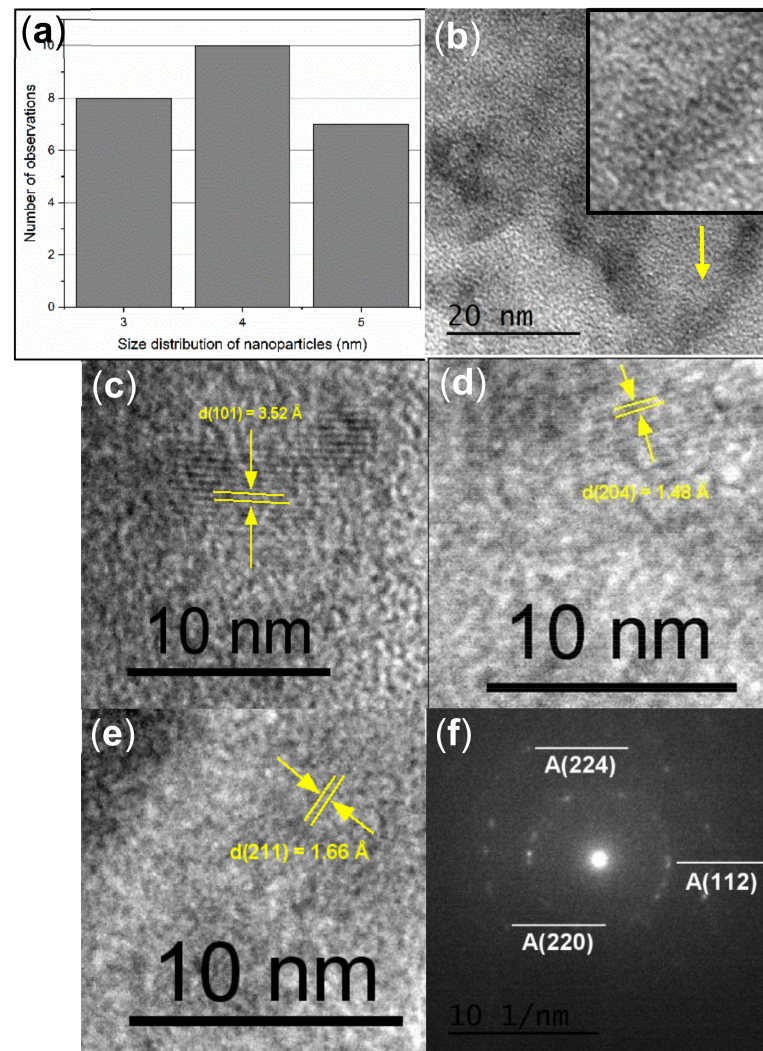


**Figure 8.** TEM micrography of sample  $7\text{TiO}_2\text{-9SiO}_2$  (a) Size distribution of  $7\text{TiO}_2\text{-9SiO}_2$  nanoparticles on thin films. (b) The disordered wormhole-like pore structure, (c–e) High-resolution TEM micrograph of  $7\text{TiO}_2\text{-9SiO}_2$  thin films; crystalline planes are observed. This Figure shows the inter-planar distance obtained from various zones of the sample. (f) SAED pattern of  $7\text{TiO}_2\text{-9SiO}_2$  thin films indexed using anatase  $\text{TiO}_2$  crystallographic parameters.

### 3.7. Degradation of MB with $\text{SiO}_2\text{-TiO}_2$ Photocatalyst under UV Irradiation

The main by-products and most worrying pollutants in the textile industry are organic dyes, which are known to degrade when exposed to high levels of photocatalytic activity (PA) in mesoporous  $\text{TiO}_2$ . It is particularly important to consider a good excitation during photocatalysis, as the energy of the  $E_g$  must be exceeded. The  $\text{TiO}_2$  anatase phase has an  $E_g$  of 3.2 eV, and the corresponding wavelength value of 387 nm showed that light with shorter wavelengths is needed for this project; a wavelength value of 254 nm was selected.  $\text{TiO}_2$  is excited by UV radiation, resulting in valence band holes that oxidize  $\text{OH}^-$  ions or  $\text{H}_2\text{O}$  to produce the hydroxyl radical ( $\cdot\text{OH}$ ) species. The compound is an extremely potent oxidant that easily oxidizes most organic molecules, converting them to  $\text{CO}_2$ , water, and salts [42]. Nevertheless, to improve the absorption efficiency of the  $\text{TiO}_2$ , it must be hydrated with

some additive, such as  $P_2O_5$ , carbon, or  $SiO_2$  [43]. In this work we have deposited  $SiO_2$  thin films on Corning glass substrates, subsequently, various layers of  $TiO_2$  were deposited. The opportunity for the hydroxyl radical ( $\cdot OH$ ) and dye molecules to react during the PA can be enhanced if the thin films absorb more color molecules. The decision was made to utilize the photodegradation of MB to assess the PA of  $TiO_2$ - $SiO_2$  thin films for dye discoloration applications. UV/Vis spectroscopy was used to determine the solution's time-dependent MB concentration. Figure 9a plots the normalized MB concentration under UV radiation as a function of time in the absence of any photocatalyst, in the presence of  $SiO_2$ , and utilizing various concentrations of thin films. The ratio of  $C_t/C_0$  at time  $t = 0$  is calculated as 1, using  $C_0$  as the initial MB concentration, and  $C_t$  corresponds to the concentration of unreacted dye at various times. Figure 9a clearly shows that while photolysis does not result in noticeable dye discoloration, MB concentration decreases roughly 20% after 5h for  $SiO_2$  films, reaching substantially more extensive and faster discoloration performances when using  $TiO_2$ - $SiO_2$  films. Since  $5TiO_2$ - $9SiO_2$  materials showed similar activity to that observed for  $9TiO_2$  thin films (in which  $SiO_2$  is not present) and since the photocatalytic activity of  $TiO_2$ - $SiO_2$  increases as the number  $TiO_2$  layers on  $SiO_2$  is larger, it is possible to suggest that  $SiO_2$  acts not only as  $TiO_2$  support in these PA films but as a functional semiconductor layer in the hetero-semiconducting film. As observed from the data in Figure 9a, increasing the number of  $TiO_2$  layers results in faster discoloration kinetic curves [44,45]. A detailed investigation of the function that particle size plays in pure  $TiO_2$  photocatalysts under UV light (wavelength 310–330 nm) was made by Zhang et al. They discovered that the kinetics of the electron/hole recombination process depended critically on particle size [44]. According to Afshar et al., the challenges brought on by the drawbacks of pure titanium powder require the manufacture of modified titania. They found that an increased surface area and interaction regions between the  $SiO_2$  and the titanium nanoparticles could result in a combined impact that can be the primary cause of the high activity of  $TiO_2$ - $SiO_2$  [45].

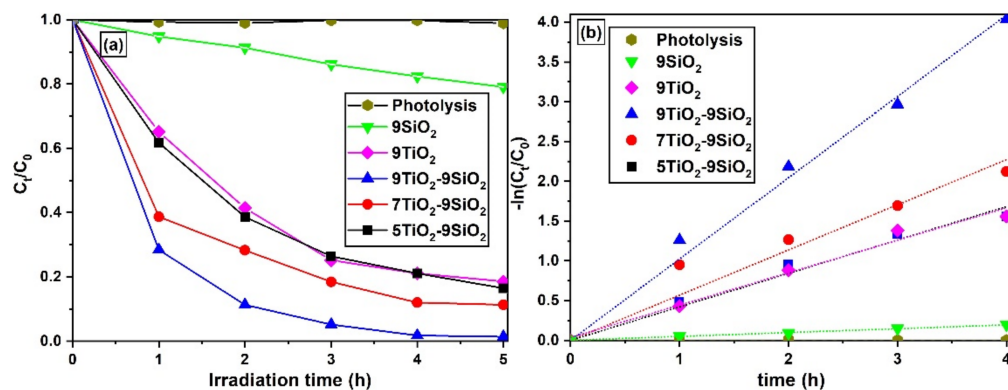


**Figure 9.** (a) Normalized concentration of MB vs UV-light irradiation time in the presence of  $TiO_2$ - $SiO_2$  thin films. (b) Reaction kinetics of MB photocatalytic degradation at different loadings of  $TiO_2$ - $SiO_2$  catalyst.

In gas-solid systems, the Langmuir-Hinshelwood (L-H) model has been successfully used to explain the kinetics of heterogeneous catalysis. This model was expanded upon by Al-Ekabi and Serpone [46] to include heterogeneous catalysis of a liquid-solid system. In order to obtain quantitative information on the photocatalytic activity of the as-prepared products, the kinetics of photocatalytic degradation of MB was also investigated. The degradation of MB can be described using the pseudo-first-order Langmuir-Hinshelwood kinetic model as shown below:

$$r = -\frac{dC}{dt} = kC^n \quad (5)$$

where  $C$  is the concentration of the solution,  $k$  is the reaction rate constant, and  $n$  is the order of the reaction. Since photocatalytic oxidation is governed by a first-order reaction, the Equation (6) is obtained:

$$-\frac{dC}{dt} = kC \quad (6)$$

Integrating the Equation (6), and using the following initial conditions,  $t = 0$ ,  $C = C_0$ ,  $C' = \ln C_0$ , we obtain the Equation (8) in which the reaction rate constant,  $k$ , allows for analysis of the efficiency of the dye degradation process.

$$-\ln C = kt + C' \quad (7)$$

$$-\ln\left(\frac{C_t}{C_0}\right) = kt \quad (8)$$

where the apparent first-order rate constant is denoted by  $k$ . With increasing  $\text{TiO}_2$ - $\text{SiO}_2$  catalyst loading, it was discovered that the rate constant  $k$  increased (Table 1). Multiple heterogeneous photocatalytic systems have used this kinetic model successfully. In Figure 9b, the curves for  $\text{SiO}_2$  and  $\text{TiO}_2$ - $\text{SiO}_2$  with varied layers are presented as  $-\ln(C_t/C_0)$  vs.  $t$ . In the presence of  $\text{TiO}_2$ , the  $\text{SiO}_2$  thin films photocatalytic activity is enhanced [47].  $\text{SiO}_2$  thin films have the ability to become acidic, which increases the amount of surface hydroxyl groups [48]. Moreover, surface hydroxyl groups have the ability to take up photoinduced holes from  $\text{TiO}_2$  to produce OH radicals, which can then oxidize absorbed molecules. Hence, Bronsted acidity can be mostly responsible for the increased  $\text{TiO}_2$ - $\text{SiO}_2$  activity, which is consistent with the earlier result by Lu et al. [49]. Simultaneously, it was found that the photocatalytic activity of  $\text{SiO}_2$  could be significantly improved by depositing  $\text{TiO}_2$  thin films on it. As seen in Figure 9b, photocatalysts made of 9 $\text{TiO}_2$ -9 $\text{SiO}_2$  are substantially more active than  $\text{SiO}_2$  at degrading MB.

**Table 1.** Results of the photodegradation of MB.

Sample	$k$ ( $\text{h}^{-1}$ )	$R^2$	Degradation (%)
9 $\text{SiO}_2$	0.048	0.997	21
9 $\text{TiO}_2$	0.406	0.982	82
5 $\text{TiO}_2$ -9 $\text{SiO}_2$	0.397	0.982	83
7 $\text{TiO}_2$ -9 $\text{SiO}_2$	0.498	0.956	89
9 $\text{TiO}_2$ -9 $\text{SiO}_2$	0.978	0.993	98

### 3.8. Photocatalytic Mechanism

Figure 10a shows a band diagram illustrating the energy levels of the conduction and valence bands for  $\text{TiO}_2$  and  $\text{SiO}_2$ . It is important to point out that the conduction band energy of  $\text{TiO}_2$  is lower than that of  $\text{SiO}_2$ ; therefore, photo-excited electrons on both semiconductor layers are readily transferred to the conduction band of  $\text{TiO}_2$ . Inspection of the energy band positions and scheme in Fig 10 also shows that photo-generated holes are promoted to the valence band of  $\text{TiO}_2$  where interphasial oxidation reactions may occur (in Figure 10b this hole-induced oxidation mechanism for methylene blue (MB) is depicted).

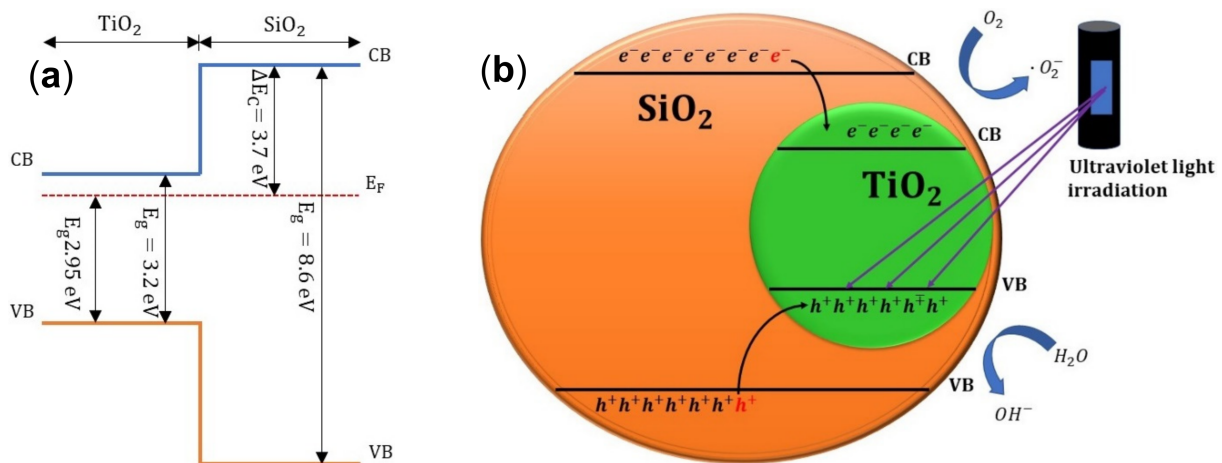


**Figure 10.** (a) TiO<sub>2</sub>-SiO<sub>2</sub> Band diagram. ΔCB and ΔVB denote the conduction and valence band offset between SiO<sub>2</sub> and TiO<sub>2</sub>, respectively, and E<sub>F</sub> denote the Fermi level. (b) Photodegradation mechanism of TiO<sub>2</sub>-SiO<sub>2</sub> under UV light irradiation.

In this way, when the photocatalyst absorbs a photon with energy equal to or greater than the band gap energy, the photogenerated electrons and holes are efficiently separated by the space-charge layer, with the holes being transported to the TiO<sub>2</sub> surface. The primary photon energy-derived elements that interact with H<sub>2</sub>O or OH<sup>-</sup> adsorbed on the surface to make ·OH are called photogenerated holes [50–52]. As can be seen from Figure 10b and the equations that follow:



The superoxide radicals (·O<sub>2</sub><sup>-</sup>), which are highly oxidant species, are created when the photogenerated electrons interact with the O<sub>2</sub> on the surface. In fact, these reactions produce a variety of active free radicals with high oxidizing characteristics, such as (·OH, ·O<sub>2</sub><sup>-</sup>, and HOO·). It should be highlighted, too, that the high rate of photogenerated e<sup>-</sup> h<sup>+</sup> recombination makes less effective photodegradation of challenging contaminants. According to [53,54], the interaction between TiO<sub>2</sub> and SiO<sub>2</sub> improves the separation of charge carriers (e<sup>-</sup> and h<sup>+</sup>) and makes it easier for them to transfer between one another. As a result, the suppression of electron-hole recombination is only partially effective, leading to an increase in photoactivity.

#### 4. Conclusions

The TiO<sub>2</sub>-SiO<sub>2</sub> thin films' structural, optical, and photocatalytic properties are synthesized and evaluated in this work, as well as the significance and importance of TiO<sub>2</sub> modified SiO<sub>2</sub> substrates. It has been demonstrated that TiO<sub>2</sub>-SiO<sub>2</sub> thin films have high photocatalytic performance for the discoloration of Methylene Blue solutions, and likely for many diverse types of organic contaminants in aqueous effluents. The presence of the TiO<sub>2</sub> layers on top of SiO<sub>2</sub> thin films improved the photocatalytic properties of the films, due to the photo-generated electrons gathered in the TiO<sub>2</sub> conduction band and were drawn to the SiO<sub>2</sub> trap level, which inhibited the recombination of electrons and holes. The presence of nine layers of TiO<sub>2</sub> in the surface of SiO<sub>2</sub> yielded superior photocatalytic activity to the other samples. In the end, effective degradation of the model dye was achieved, which is crucial for the detoxification of water. In the future, by further controlling nanocrystals sizes and layers and mesopore sizes precisely, we can expect enhanced photocatalytic properties.

**Author Contributions:** Y.d.J.A.-S.: Conceived and designed the experiments, Research, Writing—original draft. M.T.-A.: Analyzed and interpreted the data, analysis tools or data. S.G.-H.: Research, proofreading. L.A.G.: Proofreading, Supervision. A.M.-L.: Conceptualization, Research, Supervision, Proofreading and editing. All authors have read and agreed to the published version of the manuscript.

**Funding:** This research received no external funding.

**Data Availability Statement:** The datasets used and/or analyzed during the current study are available from the corresponding author on reasonable request.

**Acknowledgments:** The authors would like to thank all members of the NanoBiotechnology and Photocatalysis Laboratory at Airport Campus of the Autonomous University of Querétaro.

**Conflicts of Interest:** The authors declare that they have no known competing financial interests or personal relationships that could have appeared to influence the work reported in this paper.

## References

1. Vaiano, V.; Sacco, O.; Sannino, D.; Ciambelli, P. Nanostructured N-doped TiO<sub>2</sub> coated on glass spheres for the photocatalytic removal of organic dyes under UV or visible light irradiation. *Appl. Catal. B* **2015**, *170*, 153–161. [[CrossRef](#)]
2. Bayomie, O.S.; Kandeel, H.; Shoeib, T.; Yang, H.; Youssef, N.; El-Sayed, M.M.H. Novel approach for effective removal of methylene blue dye from water using fava bean peel waste. *Sci. Rep.* **2020**, *10*, 7824. [[CrossRef](#)] [[PubMed](#)]
3. Guidolin, T.O.; Possolli, N.M.; Polla, M.B.; Wermuth, T.B.; de Oliveira, T.F.; Eller, S.; Montedo, O.R.K.; Arcaro, S.; Cechinel, M.A.P. Photocatalytic pathway on the degradation of methylene blue from aqueous solutions using magnetite nanoparticles. *J. Clean. Prod.* **2021**, *318*, 128556.
4. Ladole, M.R.; Pokale, P.B.; Patil, S.S.; Belokar, P.G.; Pandit, A.B. Laccase immobilized peroxidase mimicking magnetic metal organic frameworks for industrial dye degradation. *Bioresour. Technol.* **2020**, *317*, 124035. [[CrossRef](#)] [[PubMed](#)]
5. Fu, Y.; Wang, L.; Peng, W.; Fan, Q.; Li, Q.; Dong, Y.; Liu, Y.; Boczkaj, G.; Wang, Z. Enabling simultaneous redox transformation of toxic chromium(VI) and arsenic (III) in aqueous media—A review. *J. Hazard. Mater.* **2021**, *417*, 126041. [[CrossRef](#)] [[PubMed](#)]
6. Landge, V.K.; Sonawane, S.H.; Sivakumar, M.; Sonawane, S.S.; Babu, G.U.B.; Boczkaj, G. S-scheme heterojunction Bi<sub>2</sub>O<sub>3</sub>-ZnO/Bentonite clay composite with enhanced photocatalytic performance. *Sustain. Energy Technol. Assess.* **2021**, *45*, 101194. [[CrossRef](#)]
7. Rayaroth, M.P.; Aravindakumar, C.T.; Shah, N.S.; Boczkaj, G. Advanced oxidation processes (AOPs) based wastewater treatment—Unexpected nitration side reactions—A serious environmental issue: A review. *Chem. Eng. J.* **2022**, *430*, 133002. [[CrossRef](#)]
8. Chen, D.; Cheng, Y.; Zhou, N.; Chen, P.; Wang, Y.; Li, K.; Huo, S.; Cheng, P.; Peng, P.; Zhang, R.; et al. Photocatalytic degradation of organic pollutants using TiO<sub>2</sub>-based photocatalysts: A review. *J. Clean. Prod.* **2020**, *268*, 121725. [[CrossRef](#)]
9. Radha, E.; Komaraiah, D.; Sayanna, R.; Sivakuma, J. Photoluminescence and photocatalytic activity of rare earth ions doped anatase TiO<sub>2</sub> thin films. *J. Lumin.* **2022**, *244*, 118727. [[CrossRef](#)]
10. Fouzia, A.; Rabah, B. The influence of doping lead and annealing temperature on grown of nanostructures of TiO<sub>2</sub> thin films prepared by a sol-gel method. *Mater. Sci. Eng. B* **2021**, *265*, 114982. [[CrossRef](#)]
11. Kamarulzaman, U.A.; Rahman, M.Y.A.; Su'ait, M.S.; Umar, A.A. Effect of annealing treatment on multilayer TiO<sub>2</sub> films on the performance of dye-sensitized solar cells. *Optik* **2020**, *218*, 164976. [[CrossRef](#)]
12. Lukong, V.T.; Ukoba, K.; Yoro, K.O.; Jen, T.C. Annealing temperature variation and its influence on the self-cleaning properties of TiO<sub>2</sub> thin films. *Heliyon* **2022**, *8*, e09460. [[CrossRef](#)]
13. Garlisi, C.; Palmisano, G. Radiation-free superhydrophilic and antifogging properties of e-beam evaporated TiO<sub>2</sub> films on glass. *Appl. Surf. Sci.* **2017**, *420*, 83–93. [[CrossRef](#)]
14. Rajput, R.B.; Jamble, S.N.; Kale, R.B. A review on TiO<sub>2</sub>/SnO<sub>2</sub> heterostructures as a photocatalyst for the degradation of dyes and organic pollutants. *J. Environ. Manag.* **2022**, *307*, 114533. [[CrossRef](#)]
15. Zhou, L.; Yan, S.; Tian, B.; Zhang, J.; Anpo, M. Preparation of TiO<sub>2</sub>-SiO<sub>2</sub> film with high photocatalytic activity on PET substrate. *Mater. Lett.* **2006**, *60*, 396. [[CrossRef](#)]
16. Ennaoui, A.; Sankapal, B.R.; Skryshevsky, V.; Lux-Steiner, M.C. TiO<sub>2</sub> and TiO<sub>2</sub>-SiO<sub>2</sub> thin films and powders by one-step soft-solution method: Synthesis and characterizations. *Sol. Energy Mater. Sol. Cells* **2006**, *90*, 1533–1541. [[CrossRef](#)]
17. Chang, W.; Yan, L.; Liu, B.; Sun, R. Photocatalytic activity of double pore structure TiO<sub>2</sub>/SiO<sub>2</sub> monoliths. *Ceram. Int.* **2017**, *43*, 5881–5886. [[CrossRef](#)]
18. Ghosh, T.B.; Dhabal, S.; Datta, A.K. On crystallite size dependence of phase stability of nano-crystalline TiO<sub>2</sub>. *J. Appl. Phys.* **2003**, *94*, 4577–4582. [[CrossRef](#)]
19. Zhang, J.; Huang, Z.; Xu, Y.; Kang, F. Carbon-coated TiO<sub>2</sub> composites for the photocatalytic degradation of low concentration benzene. *New Carbon Mater.* **2011**, *26*, 63–70. [[CrossRef](#)]
20. Torchynska, T.V.; Vazquez, A.L.Q.; Polupan, G.; Matsumoto, Y.; Khomenkova, L.; Shcherbyna, L. Correlation between the photoluminescence and different types of Si nano-clusters in amorphous silicon. *J. Non-Cryst. Solids* **2008**, *354*, 2186–2189. [[CrossRef](#)]

21. Demirkol, U.; Pat, S.; Mohammadigharehbagh, R.; Musaoğlu, C.; Özgür, M.; Elmas, S.; Özen, S.; Korkmaz, Ş. Determination of the structural, morphological, and optical properties of graphene doped SnO thin films deposited by using thermionic vacuum arc technique. *Phys. B Condens. Matter* **2019**, *569*, 14–19. [[CrossRef](#)]
22. Lin, S.S.; Huang, J.L. Effect of thickness on the structural and optical properties of ZnO films by r.f. magnetron sputtering. *Surf. Coat. Technol.* **2004**, *185*, 222–227. [[CrossRef](#)]
23. Khan, M.I.; Imran, S.; Shah Nawaz, D.; Saleem, M.; Rehman, S.U. Annealing effect on the structural, morphological, and electrical properties of TiO<sub>2</sub>/ZnO bilayer thin films. *Results Phys.* **2018**, *8*, 249–252. [[CrossRef](#)]
24. Miled, I.B.; Jlassi, M.; Sta, I.; Dhaouadi, M.; Hajji, M.; Mousdis, G.; Kompitsas, M.; Ezzaouia, H. Influence of In-doping on microstructure, optical and electrical properties of sol-gel derived CdO thin films. *J. Mater. Sci. Mater. Electron.* **2018**, *29*, 11286–11295. [[CrossRef](#)]
25. Away, R.D.Y.; Takai-Yamashita, C.; Ban, T.; Ohya, Y. Photocatalytic properties of TiO<sub>2</sub>-SiO<sub>2</sub> sandwich multilayer films prepared by sol-gel dip-coating. *Thin Solid Film.* **2021**, *720*, 138522. [[CrossRef](#)]
26. Kaveh, R.; Mokhtarifar, M.; Bagherzadeh, M.; Lucotti, A.; Diamanti, M.V.; Pedferri, M. Magnetically Recoverable TiO<sub>2</sub>/SiO<sub>2</sub>/γ-Fe<sub>2</sub>O<sub>3</sub>/rGO Composite with Significantly Enhanced UV-Visible Light Photocatalytic Activity. *Molecules* **2020**, *25*, 2996. [[CrossRef](#)]
27. Hao, B.; Guo, J.; Zhang, L.; Ma, H. Magnetron sputtered TiO<sub>2</sub>/CuO heterojunction thin films for efficient photocatalysis of Rhodamine B. *J. Alloy. Compd.* **2022**, *903*, 163851. [[CrossRef](#)]
28. Amano, F.; Nakata, M.; Yamamoto, A.; Tanaka, T. Rutile titanium dioxide prepared by hydrogen reduction of Degussa P25 for highly efficient photocatalytic hydrogen evolution. *Catal. Sci. Technol.* **2016**, *6*, 5693–5699. [[CrossRef](#)]
29. Xie, W.; Li, R.; Xu, Q. Enhanced photocatalytic activity of Se-doped TiO<sub>2</sub> under visible light irradiation. *Sci. Rep.* **2018**, *8*, 8752. [[CrossRef](#)]
30. Khan, M.I.; Bhatti, K.A.; Qindeel, R.; Althobaiti, H.S.; Alonizan, N. Structural, electrical and optical properties of multilayer TiO<sub>2</sub> thin films deposited by sol-gel spin coating. *Results Phys.* **2017**, *7*, 1437–1439. [[CrossRef](#)]
31. Fakhrutdinova, E.D.; Shabalina, A.V.; Gerasimova, M.A.; Nemoykina, A.L.; Vodyankina, O.V.; Svetlichnyi, V.A. Highly Defective Dark Nano Titanium Dioxide: Preparation via Pulsed Laser Ablation and Application. *Materials* **2020**, *13*, 2054. [[CrossRef](#)] [[PubMed](#)]
32. Martínez, H.; Cáceres, M.F.; Martínez, F.; Páez-Mozo, E.A.; Valangec, S.; Castellanos, N.J.; Molina, D.; Barrault, J.; Arzoumanian, H. Photo-epoxidation of cyclohexene, cyclooctene and 1-octene with molecular oxygen catalyzed by dichloro dioxo-(4,4'-dicarboxylato-2,2'-bipyridine) molybdenum(VI) grafted on mesoporous TiO<sub>2</sub>. *J. Mol. Catal. A Chem.* **2016**, *423*, 248–255. [[CrossRef](#)]
33. Frank, O.; Zukalova, M.; Laskova, B.; Kürti, J.; Koltai, J.; Kavan, L. Raman spectra of titanium dioxide (anatase, rutile) with identified oxygen isotopes (16, 17, 18). *Phys. Chem. Chem. Phys.* **2012**, *14*, 14567–14572. [[CrossRef](#)]
34. Ekoi, E.J.; Gowen, A.; Dorrepaal, R.; Dowling, D.P. Characterisation of titanium oxide layers using Raman spectroscopy and optical profilometry: Influence of oxide properties. *Results Phys.* **2019**, *12*, 1574–1585. [[CrossRef](#)]
35. Porto, S.P.S.; Fleury, P.A.; Damen, T.C. Raman Spectra of TiO<sub>2</sub>, MgF<sub>2</sub>, ZnF<sub>2</sub>, FeF<sub>2</sub>, MnF<sub>2</sub>. *Phys. Rev.* **1967**, *154*, 522–526. [[CrossRef](#)]
36. Tompsett, G.A.; Bowmaker, G.A.; Cooney, R.P.; Metson, J.B.; Rodgers, K.A.; Seakins, J.M. The Raman spectrum of brookite, TiO<sub>2</sub> (Pbc<sub>2</sub>, Z = 8). *J. Raman Spectrosc.* **1995**, *26*, 57–62. [[CrossRef](#)]
37. Stathatos, E.; Lianos, P.; DelMonte, F.; Levy, D.; Tsiourvas, D. Formation of TiO<sub>2</sub> Nanoparticles in Reverse Micelles and Their Deposition as Thin Films on Glass Substrates. *Langmuir* **1997**, *13*, 4295–4300. [[CrossRef](#)]
38. Yu, J.C.; Yu, J.; Zhao, J. Enhanced photocatalytic activity of mesoporous and ordinary TiO<sub>2</sub> thin films by sulfuric acid treatment. *Appl. Catal. B Environ.* **2002**, *36*, 31–43. [[CrossRef](#)]
39. Stathatos, E.; Lianos, P.; Falaras, P.; Siokou, A. Photocatalytically Deposited Silver Nanoparticles on Mesoporous TiO<sub>2</sub> Films. *Langmuir* **2000**, *16*, 2398–2400. [[CrossRef](#)]
40. Haapanen, J.; Aromaa, M.; Teisala, H.; Tuominen, M.; Stepien, M.; Saarinen, J.J.; Heikkilä, M.; Toivakka, M.; Kuusipalo, J.; Makela, J.M. Binary TiO<sub>2</sub>/SiO<sub>2</sub> nanoparticle coating for controlling the wetting properties of paperboard. *Mater. Chem. Phys.* **2015**, *149–150*, 230–237. [[CrossRef](#)]
41. Yu, B.; Leung, K.M.; Guo, Q.; Lau, W.M.; Yang, J. Synthesis of Ag-TiO<sub>2</sub> composite nano thin film for antimicrobial application. *Nanotechnology* **2011**, *22*, 115603. [[CrossRef](#)]
42. Pelaez, M.; Nolan, N.T.; Pillai, S.C.; Seery, M.K.; Falaras, P.; Kontos, A.G.; Dunlop, P.S.M.; Hamilton, J.W.J.; Byrne, J.A.; O'Shea, K.; et al. A review on the visible light active titanium dioxide photocatalysts for environmental applications. *Appl. Catal. B Environ.* **2012**, *125*, 331–349. [[CrossRef](#)]
43. Suzuki, N.; Jiang, X.; Radhakrishnan, L.; Takai, K.; Shimasaki, K.; Huang, Y.-T.; Miyamoto, N.; Yamauchi, Y. Hybridization of Photoactive Titania Nanoparticles with Mesoporous Silica Nanoparticles and Investigation of Their Photocatalytic Activity. *Bull. Chem. Soc. Jpn.* **2011**, *84*, 812–817. [[CrossRef](#)]
44. Zhang, Z.; Wang, C.; Zakaria, R.; Ying, J. Role of Particle Size in Nanocrystalline TiO<sub>2</sub>-Based Photocatalysts. *J. Phys. Chem. B* **1998**, *102*, 10871–10878. [[CrossRef](#)]
45. Afshar, S.; Jahromi, H.S.; Jafari, N.; Ahmadi, Z.; Hakimizadeh, M. Degradation of malachite green oxalate by UV and visible lights irradiation using Pt/TiO<sub>2</sub>/SiO<sub>2</sub> nanophotocatalyst. *Sci. Iran.* **2011**, *18*, 772–779. [[CrossRef](#)]
46. Al-Ekabi, H.; Serpone, N. Kinetic studies in heterogeneous photocatalysis. 1. Photocatalytic degradation of chlorinated phenols in aerated aqueous solution over TiO<sub>2</sub> supported on glass matrix. *J. Phys. Chem.* **1988**, *92*, 5726–5731. [[CrossRef](#)]

47. Yadav, H.M.; Kim, J.S. Fabrication of SiO<sub>2</sub>/TiO<sub>2</sub> double layer thin films with self-cleaning and photocatalytic properties. *J. Mater. Sci. Mater. Electron.* **2016**, *27*, 10082–10088. [[CrossRef](#)]
48. Fu, X.; Clark, L.A.; Yang, Q.; Anderson, M.A. Enhanced photocatalytic performance of titania-based binary metal oxides: TiO<sub>2</sub>/SiO<sub>2</sub> and TiO<sub>2</sub>/ZrO<sub>2</sub>. *Environ. Sci. Technol.* **1996**, *30*, 647–653. [[CrossRef](#)]
49. Lu, J.; Kosuda, M.; Van Duyn, R.P.; Stair, P.C. Surface acidity and properties of TiO<sub>2</sub>/SiO<sub>2</sub> catalysts prepared by atomic layer deposition: UV-visible diffuse reflectance, DRIFTS, and visible Raman spectroscopy. *J. Phys. Chem. C* **2009**, *113*, 12412–12418. [[CrossRef](#)]
50. Gao, R.Q.; Sun, Q.; Fang, Z.; Li, G.T.; Jia, M.Z.; Hou, X.M. Preparation of nano-TiO<sub>2</sub>/diatomite-based porous ceramics and their photocatalytic kinetics for formaldehyde degradation. *Int. J. Miner. Metall. Mater.* **2018**, *25*, 73–79. [[CrossRef](#)]
51. Gnanaprakasam, A.; Sivakumar, V.M.; Sivayogavalli, P.L.; Thirumarimurugan, M. Characterization of TiO<sub>2</sub> and ZnO nanoparticles and their applications in photocatalytic degradation of azodyes. *Ecotoxicol. Environ. Saf.* **2015**, *121*, 121–125. [[CrossRef](#)] [[PubMed](#)]
52. Guo, Q.; Zhou, C.; Ma, Z.; Yang, X. Fundamentals of TiO<sub>2</sub> Photocatalysis: Concepts, Mechanisms, and Challenges. *Adv. Mater.* **2019**, *31*, e1901997. [[CrossRef](#)] [[PubMed](#)]
53. Nabih, S.; Shalan, A.E.; Serea, E.S.A.; Goda, M.A.; Sanad, M.F. Photocatalytic performance of TiO<sub>2</sub>@SiO<sub>2</sub> nanocomposites for the treatment of different organic dyes. *J. Mater. Sci. Mater. Electron.* **2019**, *30*, 9623–9633. [[CrossRef](#)]
54. Gholami, T.; Bazarganipour, M.; Salavati-Niasari, M.; Bagheri, S. Photocatalytic degradation of methylene blue on TiO<sub>2</sub>@SiO<sub>2</sub> core/shell nanoparticles: Synthesis and characterization. *J. Mater. Sci. Mater. Electron.* **2015**, *26*, 6170–6177. [[CrossRef](#)]

**Disclaimer/Publisher's Note:** The statements, opinions and data contained in all publications are solely those of the individual author(s) and contributor(s) and not of MDPI and/or the editor(s). MDPI and/or the editor(s) disclaim responsibility for any injury to people or property resulting from any ideas, methods, instructions or products referred to in the content.